A Kuroshio Extension System Model Study: Decadal Chaotic Self-Sustained Oscillations

STEFANO PIERINI

Dipartimento di Scienze per l'Ambiente, Università di Napoli "Parthenope," Naples, Italy

(Manuscript received 22 February 2005, in final form 12 January 2006)

ABSTRACT

A model study of the Kuroshio Extension system, in which forcing is provided by a time-independent climatological wind, yields a mean meandering path and a decadal variability of the jet in significant agreement with in situ and altimetric measurements. A reduced-gravity primitive equation ocean model is implemented in a box spanning the whole North Pacific, including a schematic coastline at the western side, and an analytical wind forcing is determined according to the ECMWF and Comprehensive Ocean–Atmosphere Data Set (COADS) climatologies. The modeled time-averaged Kuroshio Extension shows meanders, northern and southern recirculation regions, and a jet penetration that are in good agreement with the corresponding observed climatological features. This result suggests that intrinsic nonlinear mechanisms are likely to play a major role in determining the meander pattern of the mean flow. The internal low-frequency variability is found to be a chaotic bimodal self-sustained oscillation between an energetic meandering state and a much weaker state with a reduced zonal penetration of the jet. These high and low energy states are found to be very similar to the "elongated" and "contracted" modes of the Kuroshio Extension detected through altimetric measurements; moreover, the characteristic period (of around 10 yr), flow patterns, and transition details of a typical bimodal cycle are found to be in significant agreement with altimeter observations for the period 1992–2004. A complex dynamical mechanism supporting this internal oscillation, and involving the bimodal behavior of the Kuroshio south of Japan, is proposed and discussed. On the basis of these modeling results and of their validation with altimeter data, it is hypothesized that the observed bimodal decadal variability of the Kuroshio Extension is basically due to a self-sustained internal oscillation related to the instability of the Kuroshio south of Japan without any crucial intervention of wind-driven Sverdrup transport fluctuations and of topographic interactions, although such effects certainly play an important role in shaping the finer structure of Kuroshio Extension changes. Finally, in a preliminary analysis of the variability in the framework of nonlinear dynamical systems theory it is suggested that the strange attractor corresponding to the modeled low-frequency variability is associated with a homoclinic orbit produced by a global bifurcation; moreover, transitions between oscillations of different character found for slightly different values of the lateral eddy viscosity and forcing amplitude are conjectured to be due to heteroclinic connections.

1. Introduction

The Kuroshio Extension (KE) is the eastward-flowing, free, inertial meandering jet formed by the confluence of the Kuroshio and Oyashio western boundary currents; it constitutes, therefore, a front separating the warm subtropical and cold subpolar waters of the North Pacific Ocean. The KE is a region of the World Ocean where one of the most intense air–sea heat exchanges takes place. It is also the region of the North Pacific with the highest eddy kinetic energy level (Wyrtki et al. 1976) and in which large-scale interannual changes lead to high temperature anomalies that are capable of enhancing the variability of the midlatitude coupled ocean–atmosphere system, and thus, strongly affecting North American climate (e.g., Latif and Barnett 1994, 1996; Qiu 2000). It is therefore very relevant, from a climatic point of view, to investigate the nature of the KE system. An international program, the Kuroshio Extension System Study, is currently devoted to understanding the processes that govern the variability of the KE and its interactions.

The mechanisms that generate the mean structure of the KE and its variability are not yet definitively assessed. What is the main dynamical mechanism that

Corresponding author address: Stefano Pierini, Dipartimento di Scienze per l'Ambiente, Università di Napoli "Parthenope," Via A. De Gasperi, 5-80133 Napoli, Italy.
E-mail: stefano.pierini@uniparthenope.it

produces the time-averaged meander pattern of the KE? Mizuno and White (1983) suggest that it may be due to lee-wave meanders induced by the flow of the Kuroshio over the Izu Ridge. Hurlburt et al. (1996) and Mitchell et al. (1996) also propose a mechanism based on topographic interaction, but according to their model results, the meanders are steered by eddy-driven mean abyssal currents. On the other hand, a highly nonlinear jet may develop meanders without any topographic interaction, just as a consequence of inertial effects. So the question arises as to whether internal nonlinear mechanisms may contribute (and to what extent) to determining the observed meander pattern of the KE. As for the interannual and interdecadal variability, some authors (e.g., Miller et al. 1998; Deser et al. 1999; Qiu 2002, 2003; Qiu and Chen 2005) propose that it is basically due to the external atmospheric forcing. On the other hand, it is well known that a highly nonlinear dynamical system may undergo oscillations (of periodic or chaotic nature) induced by purely internal mechanisms. So, again, the question arises as to whether the observed variability may also be affected (more or less substantially) by inertial effects.

The analysis of these dynamical aspects can advantageously rely on the development of modeling process studies specifically conceived for this oceanographic problem. The so-called double-gyre model is an ideal framework in which the dynamics of the KE can be investigated: it consists of a fluid in a box that can obey different governing equations (quasigeostrophic or shallow water equations in a reduced-gravity or layer system) and is forced by a wind field composed of two gyres representing schematically a subpolar cyclone and a subtropical anticyclone generating the corresponding oceanic gyres. This model was used in the last decade in order to investigate the internal low-frequency variability of the large-scale midlatitude ocean circulation and has introduced in physical oceanography the concepts and terminology of nonlinear dynamical systems (e.g., Jiang et al. 1995; McCalpin and Haidvogel 1996; Spall 1996a,b; Meacham 2000; Nauw and Dijkstra 2001; Ghil et al. 2002; Simonnet et al. 2003a,b; Dijkstra 2005).

In this framework, the aim of the present study is to analyze the role of nonlinear inertial effects in both the mean structure of the KE and its variability through the development of a shallow water, reduced-gravity double-gyre model. In view of the need to obtain results that, within the limits of an idealized process study, can possibly be directly comparable with observations, a double-gyre wind field and a domain of integration are used that mimic to an acceptable degree of realism the real wind and basin shape. The stationary wind field includes important meridional asymmetries inspired by European Centre for Medium-Range Weather Forecasts (ECMWF) and Comprehensive Ocean–Atmosphere Data Set (COADS) climatologies. The domain of integration has a latitudinal extension that covers the midlatitude ocean as well as an equatorial region, and its zonal extension approximates correctly the width of the North Pacific Ocean, thus insuring a fairly correct Sverdrup return flow feeding the western boundary currents (an absolutely fundamental requirement in a highly nonlinear system such as the one under investigation). Moreover, a schematic coastline at the western side of the ocean has been introduced as well. These are all features that turn out to be fundamental in producing a relatively realistic ocean circulation.

Very synthetically, we can anticipate that the obtained time-averaged KE has a structure in good quantitative agreement with observations, from which it is deduced that nonlinear inertial effects alone may play a fundamental role in determining the observed meandering structure of the mean jet. Moreover, self-sustained bimodal chaotic oscillations on a decadal time scale are obtained for the internal variability that share many important aspects with the bimodal oscillation of the KE as observed through altimetric measurements in the last 12 yr (Qiu and Chen 2005), which suggests that the internal dynamics is likely to be the main cause of the decadal variability of the KE.

The paper is organized as follows. The mathematical model and the wind forcing are presented and discussed in sections 2a and 2b, respectively. In section 3, the time-averaged KE jet obtained by the model is discussed and compared with observations and other numerical results. The internal variability is then described and an interpretation in terms of a self-sustained bimodal oscillation is proposed in section 4a, while a detailed comparison with the altimeter observations of Qiu and Chen (2005) is presented in section 4b. In section 4c a preliminary analysis of the low-frequency variability is presented in terms of nonlinear dynamical systems theory. Finally, in section 5 conclusions are drawn and future developments are outlined.

2. The model

a. The mathematical model and the domain of integration

The dynamics is described by the baroclinic system governed by the reduced-gravity nonlinear shallow water equations, representing a geophysical fluid composed of a thin upper active layer superimposed on a much deeper quiescent lower layer:

$$\mathbf{u}_t + (\mathbf{u}\cdot\nabla)\mathbf{u} + f\mathbf{k}\times\mathbf{u} = -g'\nabla\tilde{\eta} + \boldsymbol{\tau}/(\rho H) + K_H\nabla^2\mathbf{u} - \gamma\mathbf{u}|\mathbf{u}| \quad \text{and}$$

$$\tilde{\eta}_t + \nabla(H\mathbf{u}) = 0. \tag{1}$$

In (1) $\nabla = (\partial/\partial x, \partial/\partial y, 0)$, $\mathbf{k} = (0, 0, 1)$, $\boldsymbol{\tau} = (\tau_1, 0, 0)$, $\mathbf{u} = (u, v, 0)$ is the horizontal velocity vertically averaged in the upper active layer, $\tilde{\eta}$ is the interface displacement (positive downward), $H = D + \tilde{\eta}$ is the upper layer thickness, where the undisturbed layer thickness is $D = 500$ m, the density of the upper layer is $\rho = 1.0235$ g cm^{-3} and $g' = g\,\Delta\rho/\rho$ is the reduced gravity, in which the relative variation of density between the two layers is $\Delta\rho/\rho = 0.0045$ [the choice of D, ρ, and $\Delta\rho$ was suggested by the Levitus (1982) climatological values of the basin-averaged potential density in the North Pacific Ocean]. The Coriolis parameter $f = 2\Omega_{earth}\sin\varphi$ (φ is the latitude) provides the correct value of the vertical component of the planetary vorticity on the tangent plane at any latitude, as done in Pierini (2003, 2005), unlike in previous double-gyre models, where the beta plane was considered (our choice is dictated by the very large latitudinal extension of the domain of integration, which even includes the equator). As for the dissipative terms, the lateral eddy viscosity coefficient is $K_H = 220$ m^2 s^{-1} (see section 4c for an explanation of this choice), and the quadratic interfacial friction is weighed by the coefficient $\gamma = 5\times10^{-4}$. Finally, the sea surface height (SSH) η (positive upward) can be obtained from $\tilde{\eta}$ through the relation $\eta \cong \tilde{\eta}\Delta\rho/\rho$. For the computational details see Pierini (2003). The spatial and temporal grid steps are $\Delta x = \Delta y = 20$ km and $\Delta t = 20$ min, respectively. This spatial resolution was first used by Jiang et al. (1995); Simonnet et al. (2003a,b) found that the 20-km resolution is sufficient to capture the phenomenology of the strongly nonlinear and highly unsteady flow past the first Hopf bifurcation. Finally, vanishing initial conditions are assumed and no-slip conditions along the boundaries are imposed except along the eastern boundary, where free-slip conditions are used to allow free propagation of Kelvin waves during the adjustment phase (see Pierini 2003, 2005).

The domain of integration has a latitudinal extension that ranges from $\varphi = 5°$S to $\varphi = 55°$N. Along the western side of the ocean a schematic coastline is introduced, as shown in Fig. 1c. It is composed of four segments delimited by five points: P_1 = (22°N, 122°E), P_2 = (33°N, 133.8°E), P_3 = (35°N, 140.7°E), P_4 = (42°N, 142.6°E,), P_5 = (55°N, 170.6°E) [the points are projected onto the x axis through the formula $x = r_e\cos\varphi\ \pi(\lambda - \lambda_0)/180$, where r_e is the earth's radius and $\lambda_0 = 122°$E is the westernmost latitude, and to help identify the geographical position of each point the real coastline is drawn]. The first segment (P_1–P_2) starts from southern Taiwan (P_1) and reaches the island of Shikoku (P_2) bordering the East China Sea along the Ryukyu Islands. The second segment (P_2–P_3) links Shikoku with the eastern part of Honshu, off the Boso peninsula (P_3). The third segment (P_3–P_4) ends south of Hokkaido (P_4) and, finally, the fourth segment (P_4–P_5) borders the Kurile Islands and ends in the Bering Sea, northeast of the Kamchatka Peninsula (note that the lines x = const do not coincide exactly with the meridians far from $\varphi = 35°$N because of the adopted projection).

Numerical experiments (not shown) in which a straight western meridional boundary was adopted yielded a mean KE very similar to the one produced by the present implementation, but the corresponding low-frequency variability was found to be very different from that discussed in section 4: it was remarkably less realistic (in view of the altimeter measurements referred to in section 4b) as the variability was much weaker, with a different spectral structure and with very different properties in terms of dynamical systems theory. In other double-gyre model studies the importance of a schematic coastline was recognized. Spall (1996a,b) introduced a sloping coastline in the western part of the domain in order to represent the continent of the United States in a study of the Gulf Stream. Qiu and Miao (2000) discussed the importance of a realistic inclination of the Japanese coast in regional model studies of the Kuroshio south of Japan. All of this points to the importance of introducing, in double-gyre models of the wind-driven ocean circulation geometrical elements of realism (apart from more realistic wind fields), if direct comparison with observations is the goal.

Finally, the zonal extension is chosen as follows. At 35°N (the most significant latitude in this study), the Pacific Ocean extends from $\lambda \sim 140°$E to $\lambda \sim 120°$W; that is, for about 100° in longitude, corresponding to about 9000 km at that latitude. The zonal width of the domain was therefore chosen so as to extend for a length $L = 9000$ km east of point P_3, for a total length $L_x = 10700$ km.

It should be noticed that a correct choice of the zonal width is very important because, for a given wind stress curl distribution, L determines the total meridional Sverdrup transport and, as a consequence, the (opposite) net western boundary current transport. Modeling correctly the intensity of the latter is fundamental, as in a highly nonlinear dynamics such as the one under investigation incorrect values would strongly affect the realism of the modeled KE The large latitudinal extension adopted in this study is important for the same

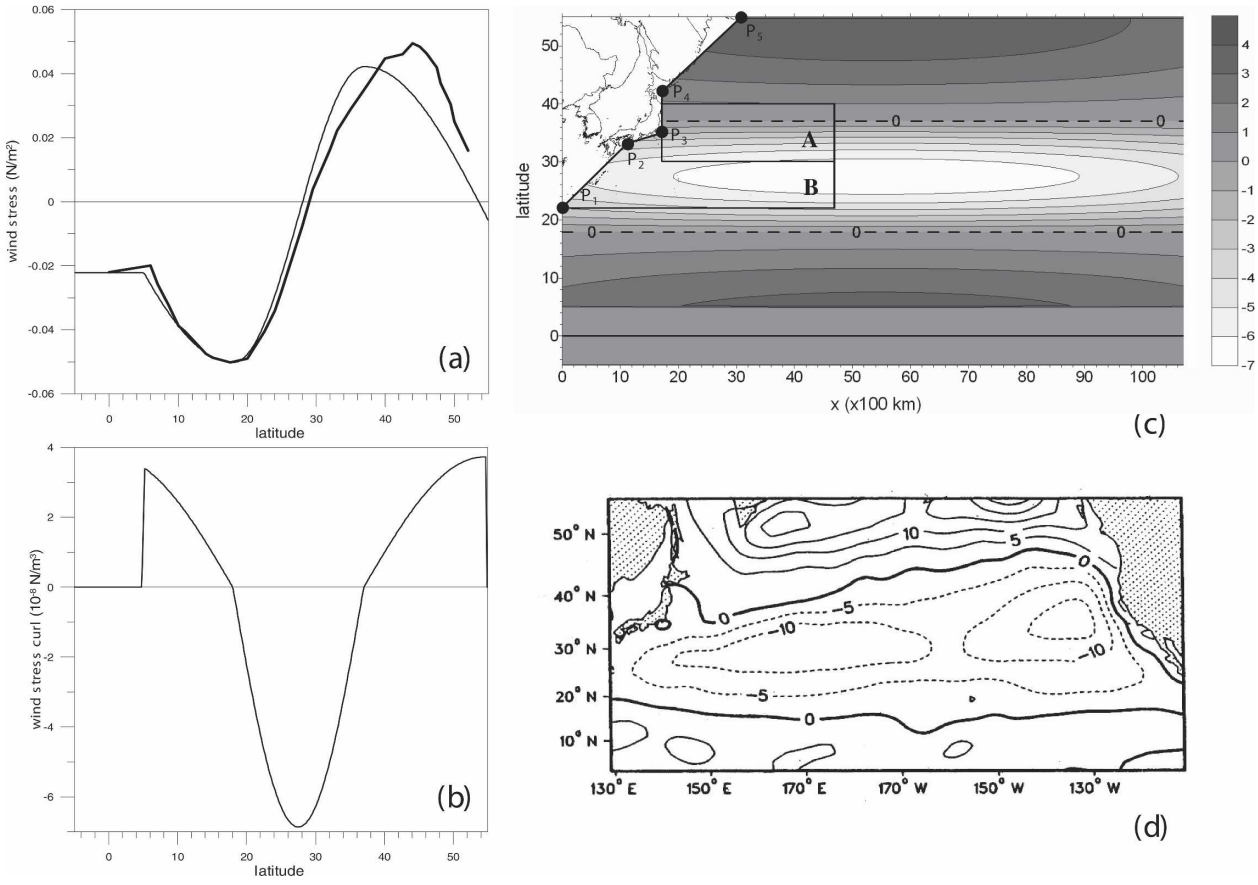

FIG. 1. (a) Thick line: meridional profile of the annual mean zonal wind stress over the North Pacific Ocean obtained by Pierini (2003) by averaging the summer and winter 10-m ECMWF climatologies as digitized from Fig. 5 of Rienecker et al. (1996); thin line: meridional profile of the zonal wind stress at $x = L_x/2$ used to force the model [Eq. (2)]. (b) Meridional profile at $x = L_x/2$ of the analytical wind stress curl. (c) Domain of integration and contour map of the analytical wind stress curl (units in 10^{-8} N m^{-3}). (d) Mean wind stress curl calculated from the COADS (from Fig. 1 of Rienecker and Ehret 1988; units in 10^{-8} N m^{-3}).

reason, since limiting meridionally the subtropical-subpolar gyres leads inevitably to a spurious decrease of the western boundary current transport.

b. The wind forcing

As mentioned in the introduction, our model of the KE should, despite its idealized nature, produce results that could (possibly) be directly compared with experimental data. The first element that must be introduced in this approach is the size (both meridional and zonal) and shape of the domain, as just discussed. The second fundamental element is the use of a wind stress field that retain a basic double-gyre structure, but that also include quantitative aspects of the real atmospheric wind forcing.

To do so we follow Pierini (2003) in defining an analytical approximation of the meridional variation of zonal winds obtained from wind analysis in the North Pacific. In that study the meridional zonally averaged, zonal 10-m ECMWF wind stress profiles obtained by Rienecker et al. (1996) were digitized for the winter and summer seasons. An approximation of the annual mean zonal wind stress over the North Pacific Ocean was then obtained by averaging the two profiles (the thick line in Fig. 1a). In the study of Pierini (2003) this mean value was used only to compute the wind variability (which was then approximated analytically), since in that model, no mean wind was included in the forcing. In the present study, on the contrary, no temporal variability is included in the forcing while that mean wind profile will be the starting point for the construction of our time-independent forcing. The thick line of Fig. 1a represents an approximation of zonally averaged winds over the North Pacific; since, however, we are interested in modeling the KE, a better representation of the winds in the western part of the basin would be desirable. Let us see how it is possible to adjust the profile for this purpose.

Figure 1d (taken from Rienecker and Ehret 1988) shows the mean wind stress curl calculated from monthly averaged stress for the period 1960–1979 from the COADS). From this map one can see that the wind profile of Fig. 1a (which has a relative minimum at $\varphi \cong 18°$ and a relative maximum at $\varphi \cong 44°$) is best representative of the central and eastern part of the basin, where (Fig. 1d) the lines of vanishing wind stress curl lay at $\varphi \cong 16°$–$18°$N and at $\varphi \cong 45°$–$48°$N and the wind stress curl values are (in module) higher in the subpolar low (steeper wind stress for $\varphi > 44°$ in the thick line of Fig. 1a) than in the subtropical high (less steep wind stress for $\varphi < 44°$ in the thick line of Fig. 1a).

In the western side of the ocean, on the other hand, such agreement is less valid for two main reasons. First, the line of vanishing wind stress curl that separates the two gyres is located more south, at $\varphi \cong 35°$–$40°$N, and, secondly, the wind stress curl has higher values (in module) south of that line rather than north of it. To take into account these two corrections to the profile given by the thick line of Fig. 1a, the following analytic expression for the wind stress was determined (shown by the thin line of Fig. 1a):

$$\tau_1(x, \varphi) = \alpha[0.0462 \cdot a(\varphi)b(x) - 0.004]N/m^2, \quad (2)$$

where the functions a and b are defined as:

$$a(\varphi) = \begin{cases} -\cos[k_2(\varphi_c - \varphi_b)]: & \varphi < \varphi_c \\ -\cos[k_2(\varphi - \varphi_b)]: & \varphi_c \le \varphi < \varphi_b \\ \cos[k_1(\varphi - \varphi_a)]: & \varphi_b \le \varphi < \varphi_a \\ \cos[k_2(\varphi - \varphi_a)]: & \varphi_a \le \varphi \end{cases}; \quad b(x) = \sin\left(\frac{\pi x}{2L_x} + \frac{\pi}{4}\right); \quad (3a)$$

$$k_1 = \frac{2\pi}{38} rad\ \deg^{-1}; \quad k_2 = \frac{2\pi}{70} rad\ \deg^{-1}; \quad \varphi_a = 37°; \quad \varphi_b = \varphi_a - \frac{\pi}{k_1}; \quad \varphi_c = 5°, \quad (3b)$$

and where $\alpha = 1$ (but different values will be considered in section 4c). The latitude of vanishing wind stress curl corresponds to $\varphi = 37°$, in better agreement with the western part of Fig. 1d, and a continuation up to $\varphi = 22°$ is performed (for $\varphi < 22°$ the thick and thin lines almost coincide). Moreover, for $\varphi > 37°$ the function is chosen less steep than for $\varphi < 37°$, in so obtaining a better approximation of the wind stress curl profile in the western part of the North Pacific Ocean (cf. Fig. 1b with Fig. 1d, western part). This meridional dependence is imposed in the middle of the basin ($x = L_x/2$) and a symmetric zonal modulation is also prescribed, as shown in Fig. 1c. Finally, it should be stressed that using a forcing in analytical form, as done here, rather than employing real wind stress data has the advantage of making this model results (like all the analyses based on double-gyre models published in the last decade) easily reproducible and subject to be generalized in future studies.

3. The mean jet

a. Experimental evidence

Before we analyze the mean KE as resulting from model simulation, let us first discuss its experimental evidence. The main features of the mean KE are effectively summarized by Tomczak and Godfrey (2002, chapter 8):

> The separation point for the Kuroshio is reached near 35°N. It defines the transition from the Kuroshio proper to the Kuroshio Extension. Flow in the Extension is basically eastward, but the injection of a strong jet into the relatively quiescent open Pacific environment causes strong instability. Two regions of north-southward shift, the 'First Crest' and the 'Second Crest,' are found between 140° and 152°E with a node near 147°E.

This is illustrated in Fig. 2 (small panel), which shows the climatological surface dynamic height obtained by Teague et al. (1990) (the vertical dotted lines located at 147° and 152°E delimit the two crests). Two large meanders (crests) are present, the first one is stronger and is just east of the separation point at 35°N, 141°E, and a second one is located west of 152°E, the two meanders being separated by a node centered around 147°E: moreover, the meridional fluctuation of the crests is almost symmetrical about 35°N with a latitudinal extension of $\sim \pm 2°$ (other notable features appear as well, but they will be discussed later in connection with model simulations). The climatology of Levitus (1982) provides basically the same result, but with a smaller meridional excursion of the meanders (see also Qiu 2000). The mean SSH of the KE was also calculated from Ocean Topography Experiment (TOPEX)/Poseidon (T/P) altimeter data (Qiu 1995, 2000). Since the mean signal is not directly available from altimeter data due to the inaccurate knowledge of the geoid, a kinematic jet model was developed for reconstructing the along-track mean SSH profile (Kelly and Gille

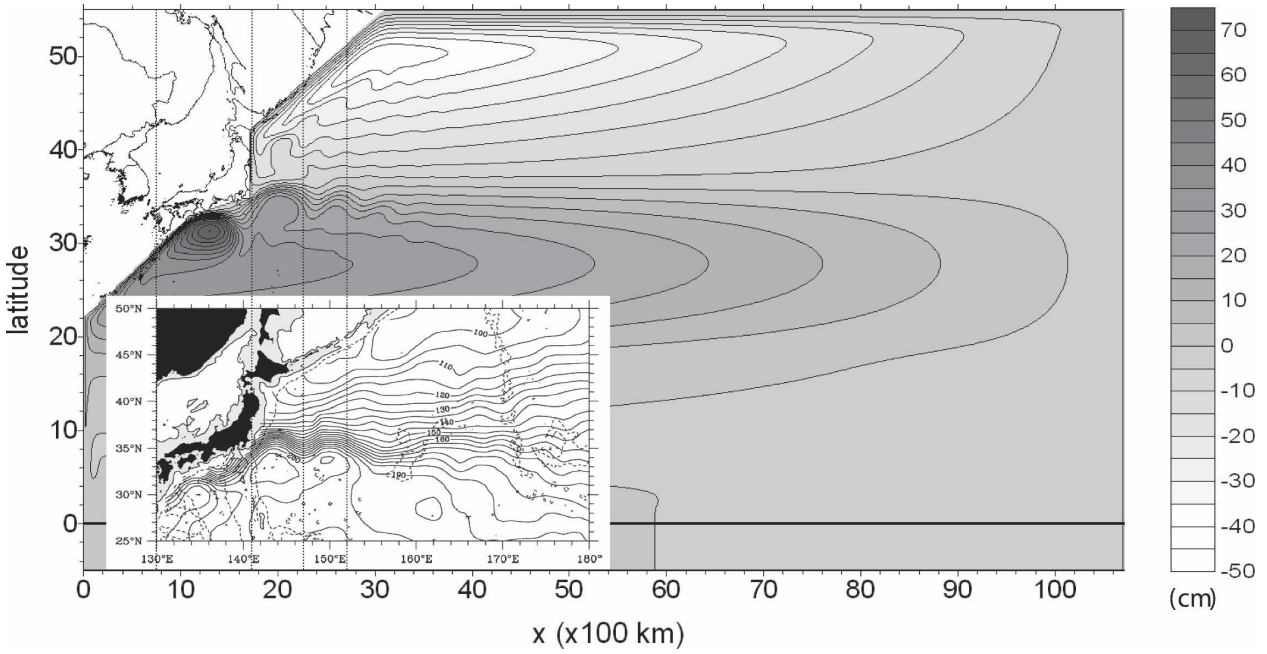

FIG. 2. Time-averaged SSH with superimposed (small panel) climatological surface dynamic height (dyn cm) relative to 1000 dbar (from Teague et al. 1990). The two pictures have the same scale along y and the same scale along x at latitudes near $\varphi = 35°$N.

1990; Qiu et al. 1991; Qiu 1995). The use of this model and of T/P data of 1992 to 1998 has produced a mean SSH field objectively mapped from the along-track mean SSH profiles (Qiu 2000) that is almost coincident with the climatologies described above. For the SSH difference δh across the KE, if one considers the first meander, a rough estimate is $\delta h \cong 50$ cm from Fig. 2 (small panel) and $\delta h \cong 70$ cm from the climatology obtained from T/P data [see Fig. 1b of Qiu (2000), but refer to the same study for a useful objective definition of a zonally averaged δh]. Finally, Lagrangian data are also available that confirm this picture of the mean KE meandering jet (Niiler et al. 2003, see in particular their Figs. 11a,b).

b. *Model simulation and comparison with observations and other numerical results*

The model response to the wind forcing given by (2) is shown in Fig. 3a in terms of the kinetic energy $E_K(t)$,

$$E_K(t) = \frac{1}{2}\int\int_{\Sigma} H|\mathbf{u}|^2\, dx\, dy;\; E_P(t) = \frac{1}{2}g'\int\int_{\Sigma}\tilde{\eta}^2\, dx\, dy \tag{4}$$

(the potential energy E_P will be used in section 4c) integrated separately in the sectors (see Fig. 1c) $\Sigma = A$ (the Kuroshio Extension region) and $\Sigma = B$ (the Kuroshio south of Japan). The simulated jet yields a chaotic bimodal oscillation on a decadal time scale due to the intrinsic nonlinear dynamics, but this will be discussed in detail in the next section. Here, the time average of the SSH over the period $t = 140$–170 years (see next section for the analysis of the variability during this interval) was computed (from now on t is the time of integration, vanishing fields corresponding to $t = 0$). The resulting mean SSH field is shown in Fig. 2 (large panel), with superimposed the climatological surface dynamic height of Teague et al. (1990) just discussed. The two pictures have the same y scale and the same x scale at latitudes near $\varphi = 35°$N (where the lines $x =$ const coincide with the meridians).

The meandering of the simulated mean jet, its downstream structure, its intensity, and the northern and southern recirculation regions appear to be in substantial agreement with the observed climatology. The point of detachment of the modeled Kuroshio is at 35°N, 141°E, in agreement with observations (note that the line of vanishing wind stress curl is imposed at 37°, so the separation line of the western boundary currents represents a nontrivial oceanic response to the winds, and clearly depends on the shape of the coastline). A first meander corresponds quite well with the observed one as far as its zonal width, curvature, location, and strength are concerned, although it is slightly weaker ($\delta h \cong 35$ cm) and extends about one degree farther eastward. The second meander is also in basic agreement with the observed one, although it appears shifted eastward by about one degree in longitude. East of the

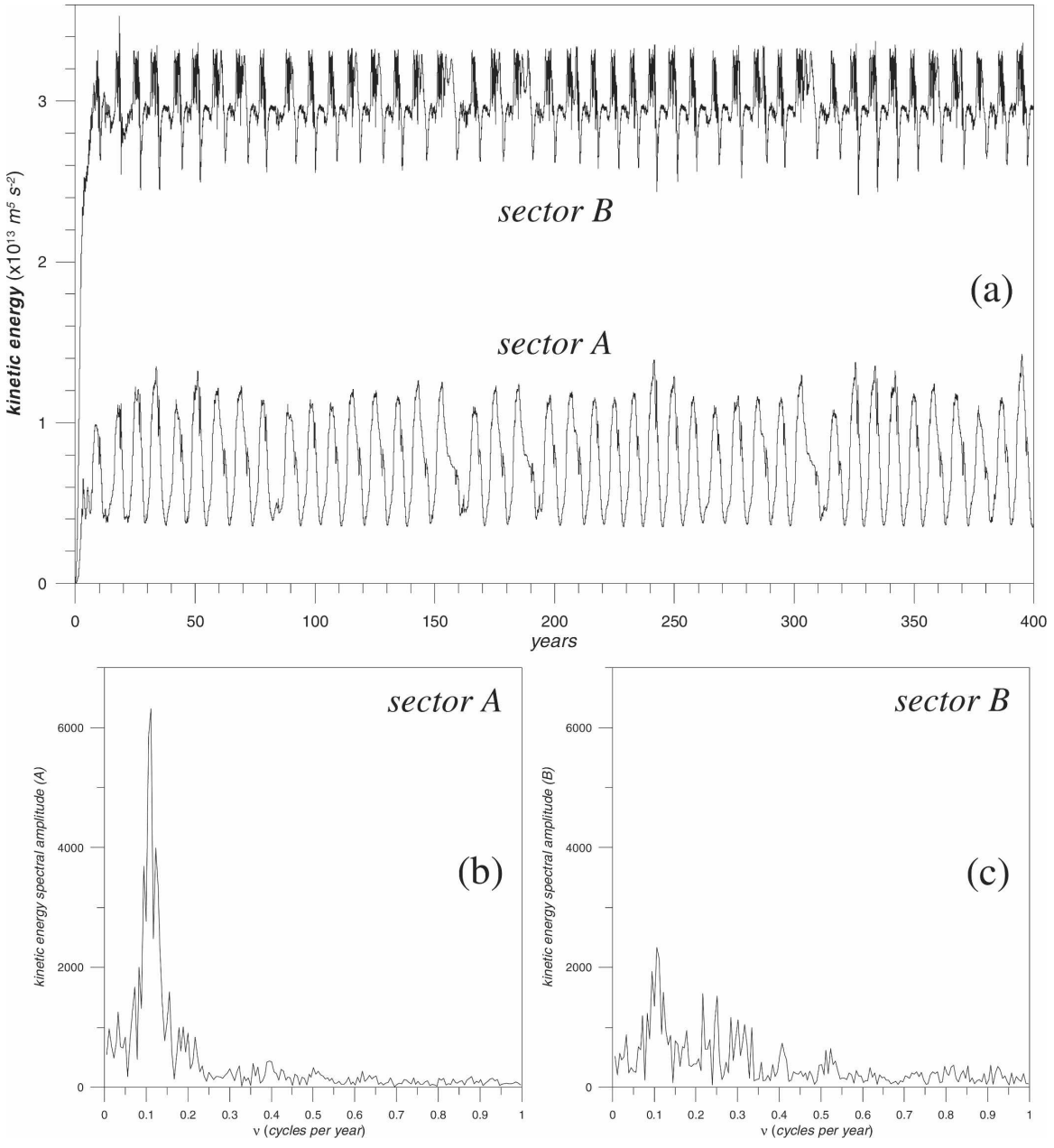

FIG. 3. (a) Time series of the kinetic energy integrated over the sectors A and B (see Fig. 1c). (b), (c) Corresponding spectral amplitudes (the mean was removed).

second crest the mean axis of the jet is slightly inclined southward in both the observed and modeled KE; a weaker meandering path about the axis of the jet is evident in both images as well, and the more intense spatial fluctuations present in the real ocean are usually accounted for topographic interactions with the Shatsky Rise and, more eastward, with the Emperor Seamounts, all effects absent in this model. The recirculation gyre south of the main meanders appears also in basic agreement with the climatological one.

Also the modeled path of the Kuroshio south of Japan shows similarities with the climatological western boundary current. Both paths present an anticyclonic recirculation gyre which, in the climatological signal lies south of 32°N and west of 137°E, while in the modeled signal it is more energetic and lies south of 33°N and west of 139°E. More to the north a cyclonic meander is present, which is reminiscent of one of the two modes of variability of the Kuroshio (Taft 1972; Qiu and Miao 2000; Schmeits and Dijkstra 2001): it is centered at

about 34°N, 138°E in the climatological path and at about 33°N, 140°E in the modeled path. Finally, another agreement worth emphasizing is the configuration of the subpolar and subtropical gyres. The northern cyclonic cell shows, in both observed and modeled data, a meridional SSH gradient that is larger than that found in the southern anticyclonic cell. This asymmetry (related to the structure of the KE itself) is to be attributed mainly to the asymmetry of the wind stress about the line of zero wind stress curl (Figs. 1a,b,c).

We can now discuss these results in connection with other model simulations. The mean meandering structure of the KE was interpreted by Mizuno and White (1983) in terms of linear stationary Rossby lee waves in uniform eastward flow induced by the interaction of the Kuroshio Current with the Izu Ridge. Hurlburt et al. (1996) presented a variety of realistic eddy-resolving models of the North Pacific Ocean: all their reduced-gravity and multilayer implementations produced KE jets not sufficiently realistic, except their ⅛° and 1/16° six-layer models with realistic bottom topography, which were able to produce a mean KE in close agreement in latitude and longitude, and in its meander pattern, with the climatology of Teague et al. (1990). The authors, therefore, concluded that topographic features (such as seamounts and features of the abyssal plain) are crucial in determining this configuration, as the eddy-driven deep mean flows generated by a mixed barotropic–baroclinic instability of the KE allow the bottom topography to steer the mean path of the KE. The model results just presented show, on the other hand, that purely nonlinear intrinsic effects (along with barotropic instability) in a dynamically active upper layer disconnected from the bottom topography are able to induce a meander pattern of the mean KE in significant agreement with the known climatology. This does not imply that topographic effects are unimportant, but rather that they may not be decisive in determining the meanders of the KE.

4. The internal low-frequency variability

We have already seen that the simulated jet, though forced by a time-independent wind, yields a chaotic bimodal oscillation on a decadal time-scale due to nonlinear inertial effects (Fig. 3). One of the main questions we are now going to answer in this section is whether such variability is similar (and to what extent) to the observed variability of the KE, or, on the contrary, it is rather different. In the first case one might conclude that nonlinear intrinsic mechanisms are important for the generation of the low-frequency variability of the jet, or, in the most extreme case, they may even be the main cause of it. In the second case nonlinear effects may well be important, but only their interaction with externally induced changes (studied, e.g., by Miller et al. 1998; Deser et al. 1999; Qiu 2002, 2003; Qiu and Chen 2005) can account for a realistic variability of the jet. We anticipate that the first case seems to hold, since the time-dependent response shows a surprising similarity with the low-frequency variability of the KE as presented in the recent revealing analysis of Qiu and Chen (2005) based on altimetric measurements of the past 12 yr.

a. Description and interpretation of the decadal self-sustained internal oscillations

Let us begin by analyzing the variability of the modeled jet and the dynamical mechanisms that produce it (comparison with observations will be considered in the next subsection). Figure 3 shows that the kinetic energy integrated in the Kuroshio Extension region (sector A) is a series of aperiodic self-sustained oscillations on a decadal time scale connecting two states of different energies, the strongest one having an energy about 3 times larger than that of the other. A bimodal behavior is clearly present throughout the whole 400-yr-long time series (the kinetic energy spectrum yielding a broad peak centered at T = 9.1 yr), and the energies of the states, the time lag between two successive homologous states and the character of the transitions can differ significantly from cycle to cycle due to the chaotic nature of the oscillations. For example, within the interval t = 140–170 yr (see also Fig. 5d) chosen as a test period, the second relative maximum in A follows the first one after ~10 yr, while the third one follows the second after ~14 yr; moreover, the peak-to-peak energy variation of the second transition is ~75% of that of the third transition. As for the energy integrated in sector B (Kuroshio south of Japan, hereafter KsJ), a bimodal behavior clearly correlated with that of sector A is present, but with very different characteristics. Moreover, whereas the ratio μ between the rms of the signal and its mean value is $\mu \sim 0.8$ in sector A, in sector B it reduces to $\mu \sim 0.15$. In addition, the transition between a high energy and a low energy state appears more complex (already in terms of the kinetic energy) than that found in sector A, as shown by the broad energy distribution in the spectrum of Fig. 3c.

In Fig. 4, 10 snapshots of the SSH from t = 143 yr to t = 152 yr in the region A ∪ B are shown in the left column; in the right column, following a useful diagnostic method proposed by Qiu and Chen (2005), the paths of the Kuroshio–Kuroshio Extension system defined by the 15 cm SSH contours are reported (each panel includes 24 lines covering 1 yr centered at the indicated

time). Figures 5c,d are enlargements (for the 30-yr interval $t = 140$–170 yr) of the time series of the kinetic energy integrated in sections B and A, respectively (see Fig. 3a for the complete time series; for comments on Figs. 5a,b, see section 4b). Finally, the dots in Fig. 5d identify the 10 snapshots presented in Fig. 4. Figures 4 and 5 are complementary and should be considered in conjunction.

It should be immediately noticed that the high energy state, represented by the flow at $t = 143$ yr and the low energy state, corresponding to $t = 148$ yr, appear to be very similar to the elongated and a contracted modes of the KE observed by Qiu (2000, 2002, 2003) through TOPEX/Poseidon altimeter data, respectively. The so-called elongated state is characterized by a stronger meandering path, a larger eastward surface transport, a greater zonal penetration, and a more northerly zonal-mean path compared to the contracted mode, all features clearly common to our high and low energy states, respectively. A more detailed comparison with observations will be presented in the next subsection.

We will now analyze in detail a typical transition between the two main states of the modeled KE by referring to the 10 snapshots reported in Fig. 4 and to Figs. 5 and 6; the description of the flow is accompanied by hypotheses about the dynamical functioning of the self-sustained oscillation. We will see that, while some gross features of the internal variability are reminiscent of the relaxation oscillations found in other double-gyre models, novel dynamical mechanisms arise that are very specific of this particular case.

1) $t = 143$–145 YR

In this phase the flow is quite stable. South of Japan a strong anticyclonic recirculation gyre is followed, to the east, by a meridionally elongated cyclonic meander produced, presumably, by the barotropic instability of the western boundary current (we emphasize that, in the present reduced-gravity model, baroclinic instability is absent). The KE is, as already noticed, a high energy, elongated mode showing three recirculating anticyclonic meanders (crests) whose amplitudes and widths decrease as the distance from Japan increases. It must be noticed that while the KsJ is virtually invariant during this interval, the KE is weakly decreasing in amplitude (see Fig. 4 and Figs. 5c,d). The following physical interpretation of this behavior is proposed. The southern recirculation gyre and the KE are, in this interval, virtually isolated dynamically by the presence of the strong cyclonic meander, which is therefore acting as a barrier. South of Japan a nearly stationary, nonlinear balance is achieved between the excess of anticyclonic relative vorticity induced by the increase of planetary vorticity attached to the water columns that move northward along the western boundary current, and the dissipation of vorticity due to the lateral eddy viscosity (Pedlosky 1987). East of Japan, on the other hand, the KE slowly weakens because the flux of negative relative vorticity coming from the south remains trapped (being dissipated) west of the cyclonic meander, so that it cannot balance dissipation of the free inertial jet.

2) $t = 146$ YR

At this time Fig. 4 shows that the southern cyclonic meander is remarkably less elongated meridionally and the first crest of the KE is much less energetic then before. Some critical phenomenon must have occurred that has so rapidly disrupted the previous relatively stable scenario. The following explanation is proposed. The quasi-equilibrium phase during the interval $t = 143$–145 yr requires that the southern recirculation gyre and first crest of the KE be sufficiently strong for the cyclonic meander to act as bearing between the two anticyclonic recirculations. The weakening of the eastern recirculation discussed above has presumably unbalanced the situation, as shown by the sequence a of Fig. 6, where it is evident that the erosion of the cyclonic meander becomes pronounced only when the first crest has weakened considerably.

3) $t = 147$ YR

Now the Kuroshio penetrates into the Pacific Ocean east of Japan, the cyclonic meander has disappeared and the KE is reduced to a single, very weak crest. This could be explained as follows. The disruption of the relatively stable phase has led to the intensification of the Kuroshio south of Japan, which, thanks also to the disappearance of the meander, can now assume a straight path that can even penetrate into the open sea. The last three snapshots of sequence a of Fig. 6 show this evolution (note that the minimum of the kinetic energy integrated in sector B at $t \approx 147$ yr shown in Fig. 5c is somewhat misleading because in this case E_K does not represent the total energy of the southern recirculation gyre, as it is the case when the meander is well developed, but only the energy of that part of the gyre that lies west of 141°E).

4) $t = 148$–150 YR

At $t = 148$ yr the kinetic energy of the KE (integrated in sector A) has reached its minimum (see Fig. 5d). From now on the KE intensifies being fed by the flux of anticyclonic relative vorticity coming from the south

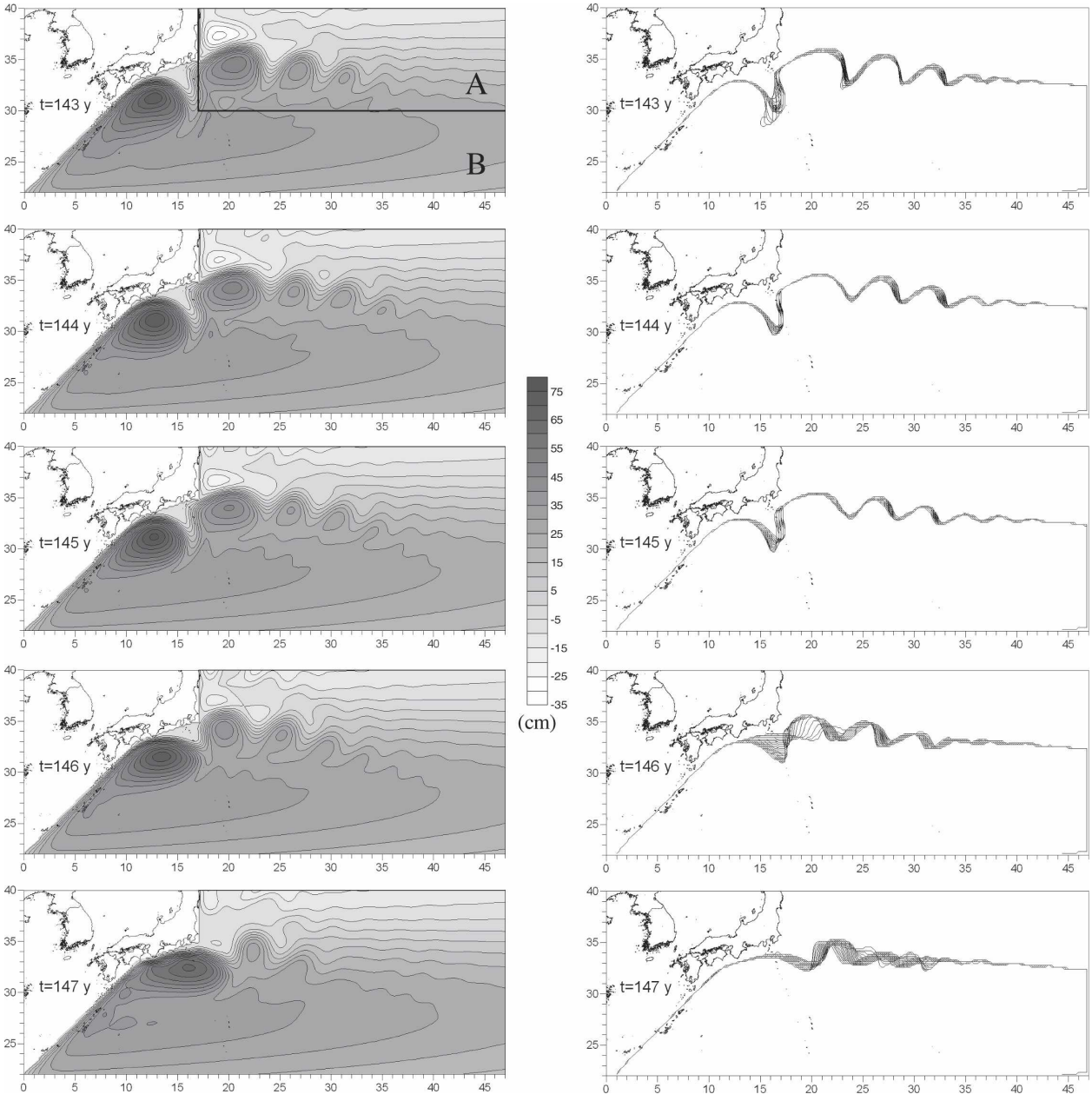

FIG. 4. (left) Snapshots of the SSH from t = 143 yr to t = 152 yr in the region A ∪ B. (right) Paths of the Kuroshio and Kuroshio Extension defined by the 15-cm SSH contours (each panel includes 24 lines covering one year centered at the indicated time).

which, in this phase, is no longer trapped in the southern recirculation gyre (whose energy remains nearly constant, as shown in Figs. 4 and 5c), because of the moderate curvature of the cyclonic meander. The gradual intensification of the KE is shown in sequence b of Fig. 6.

5) t = 151–153 YR

(The flow at t = 153 yr, not reported in Fig. 4, is virtually equal to that at t = 143 yr.) The intensification of the KE continues in this phase (the maximum kinetic energy in sector A is attained just at t = 153 yr), but it is now associated with an interesting behavior of the Kuroshio south of Japan. As soon as the meander reaches its meridionally elongated shape [at $t \approx 151$ yr, as shown by the last snapshot of sequence b of Fig. 6] it ejects a cold-core eddy that, after detaching from the meander, moves westward (see sequence c of Fig. 6). This process was actually found occurring in this region by Nishida (1982) and was modeled by Qiu and Miao

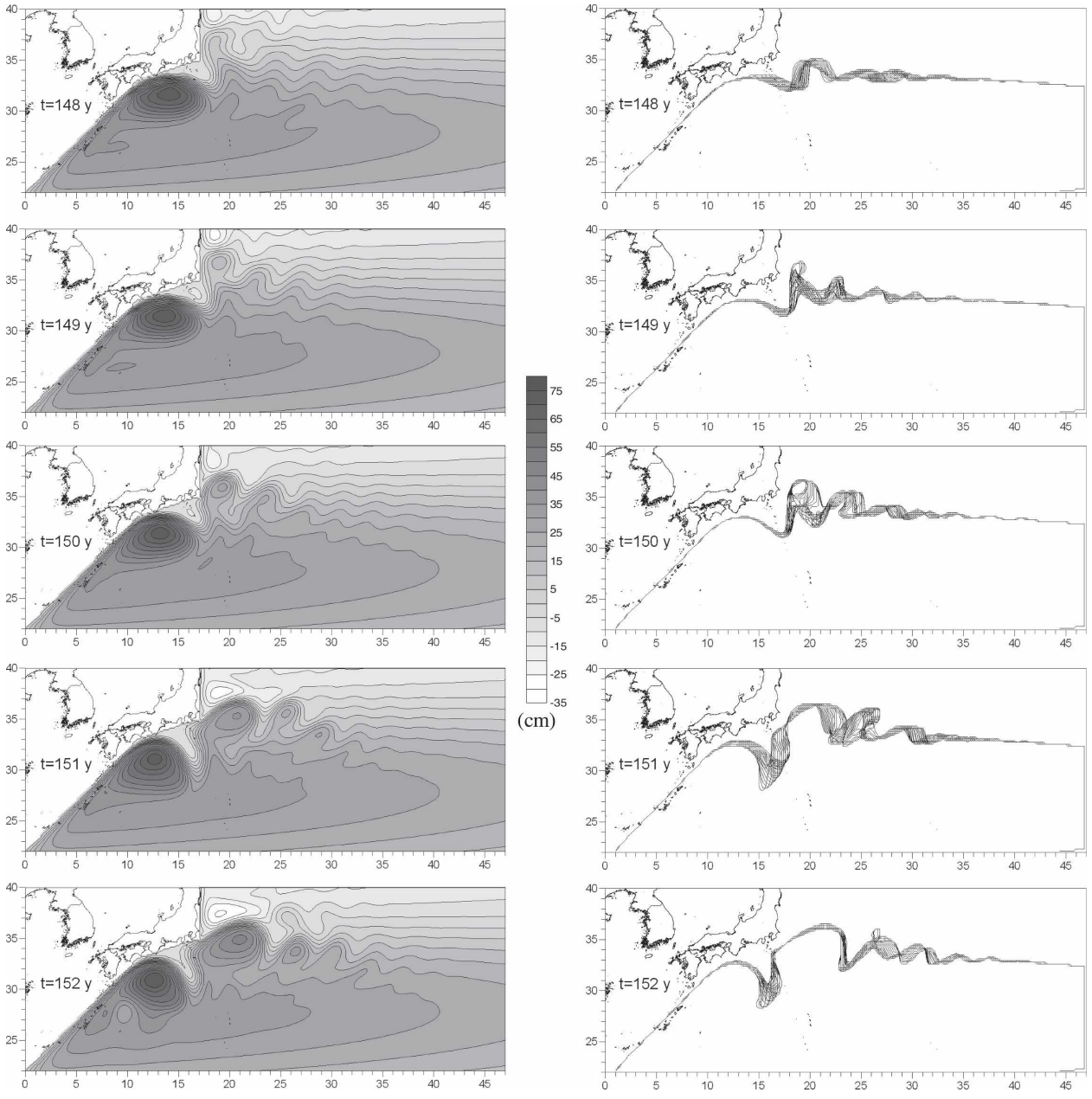

FIG. 4. (*Continued*)

(2000). Four events of this kind occur before the stable phase is achieved, corresponding to the large-amplitude oscillations in Fig. 5c within the interval $t = 151$–153 yr. It should be noticed that the shape and intensity of the southern recirculation gyre and cyclonic meander at, for instance, $t = 151$ yr are very similar to those at, for instance, $t = 143$ yr (corresponding to $t = 153$ yr), so why in the latter case the situation is stable (as discussed above) while it is strongly variable in the former, as we have just seen? Because, as we have already supposed in discussing the transition at $t \approx 146$ yr, a nearly steady western boundary current south of Japan can only be supported by a sufficiently strong "first crest" of the KE, but at $t = 151$ yr the latter is still too weak; as a consequence the excess of negative relative vorticity coming from the south actually intensifies the recirculation gyre stretching the meander, until a cyclonic eddy is detached. This leads to a strong erosion of the meander and to the beginning of a new cycle of production of a cold-core eddy. In the meantime the KE intensifies until it reaches its maximum (at $t \approx 153$ yr). At that time the stable phase of the Kuroshio south of

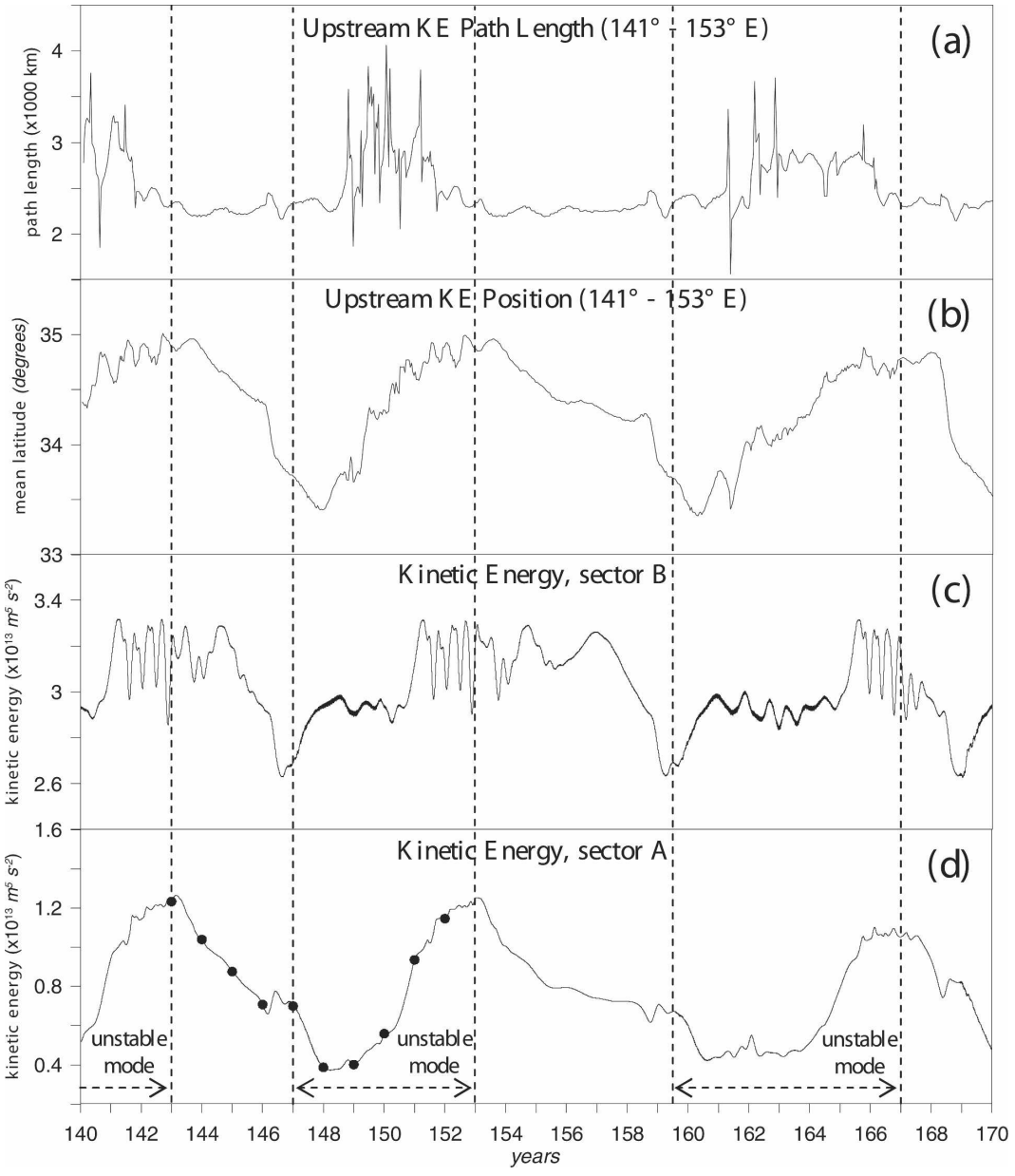

FIG. 5. Time series of (a) the Kuroshio Extension pathlength $\ell(t)$ along the 15-cm SSH isoline and of (b) the mean latitudinal position $\langle\varphi\rangle(t)$ of the latter evaluated between 141° and 153°E for the 30-yr interval t = 140–170 yr. (c), (d) Time series of the kinetic energy E_K integrated in sectors B and A, respectively. The dots in (d) identify the 10 snapshots presented in Fig. 4. The behavior between the vertical dashed lines is similar to the one identified as unstable mode by Qiu and Chen [2005, compare their Figs. 4a, c with (a), (b), respectively, according to the correspondence t = 145 yr ↔ year 1993].

Japan and the weak dissipation of the KE begins: a new decadal cycle starts.

6) FURTHER CONSIDERATIONS ABOUT THE INTERVAL t = 148–152 YR

As we have just seen, starting from t = 148 yr (when the kinetic energy of the KE is at its minimum) the KE intensifies until, at t = 152 ~ 153 yr, a fully developed (elongated) and stable KE is reached. During this interval it appears clearly from the paths in the right column of Fig. 4 (and from Fig. 5a, see section 4b) that such intensification is accompanied by a strong variability of the jet and, therefore, by high values of the eddy kinetic energy: the latter will eventually become very

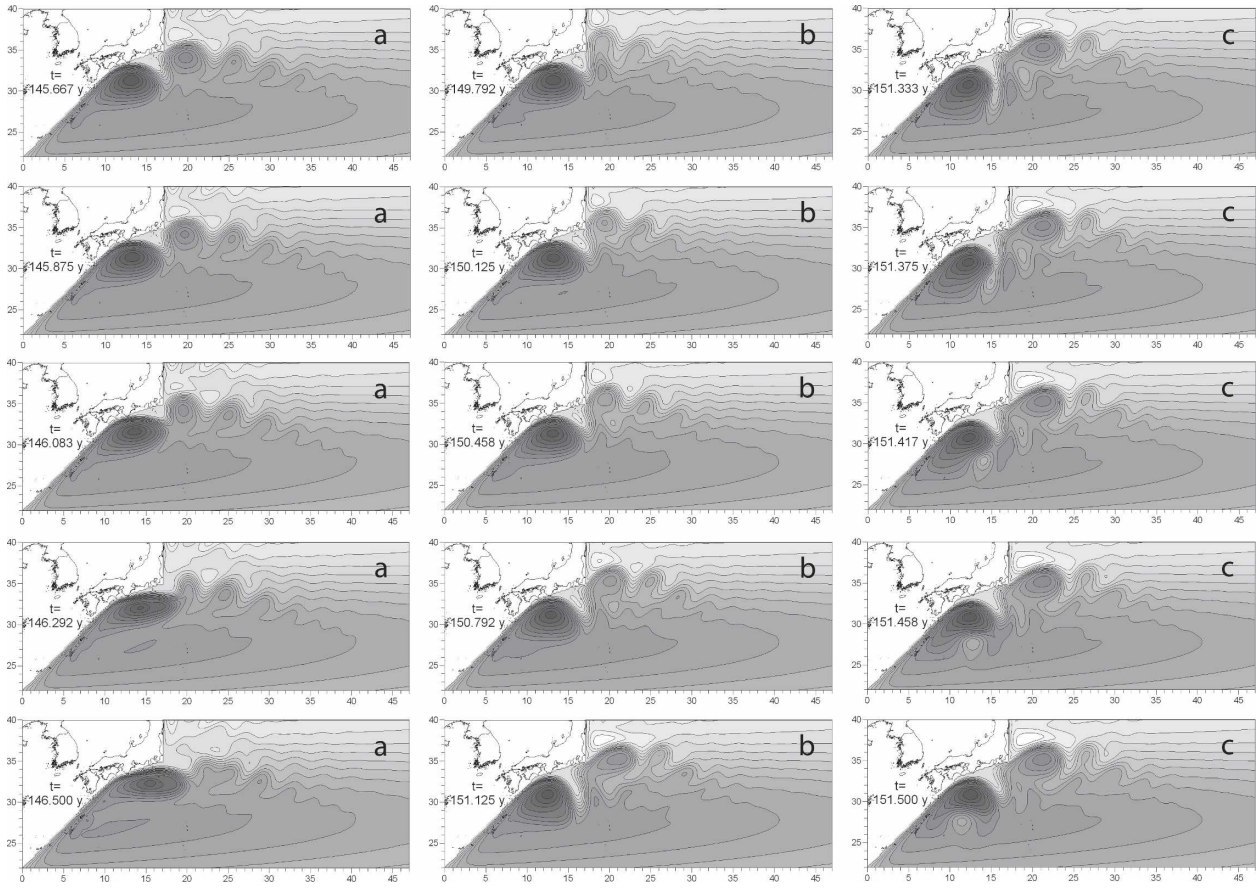

FIG. 6. Snapshots of the SSH in the region A ∪ B for three different sequences . Note the different time increment in each sequence: (a) 0.208 yr, (b) 0.333 yr, and (c) 0.042 yr. For the color bar see Fig. 4.

small during the stable phase t = 143 ~ 145 yr. This property of the jet, for which a weak (strong) KE is accompanied by high (low) values of the eddy kinetic energy was clearly observed (and with a very similar temporal evolution) from altimeter data by Qiu and Chen (2005) (see the next subsection), who judged it as counterintuitive: consequently, the possibility that such variability could be associated with instability processes was ruled out, and an explanation based on the interaction with the Izu–Ogasawara Ridge was proposed. The present modeling results suggest an alternative interpretation: the strong variability of the jet is due to the adjustment associated with the gradual intensification of the KE starting from a very weak state, without any substantial role being played by topographic interactions (that here are completely absent). Understanding the dynamical mechanisms that produce such variability is beyond the scope of this paper, but this is an interesting aspect that should be analyzed in detail in future studies.

The self-sustained internal oscillation mechanism proposed above is, in the region south of Japan, qualitatively similar to the one proposed by Qiu and Miao (2000) in order to explain the bimodal path fluctuations of the Kuroshio in the same area (as observed experimentally by Taft 1972), although the dynamical interpretations are not coincident since here the dynamics south of Japan is found to be strictly connected to that of the KE, while Qiu and Miao (2000) did not relate the latter to the former. Qiu and Miao (2000) were the first to put forward the fundamental hypothesis that the low-frequency Kuroshio variability south of Japan is not necessarily the result of a deterministic response to temporal changes of the upstream Kuroshio due to varying Sverdrup transport associated with fluctuating winds (in fact, no conclusive evidence was found of a correspondence between the Kuroshio path and the upstream inflow transport), but it could rather be due to a self-sustained internal mechanism involving the southern recirculation gyre and the stability of the Kuroshio current system. The authors then supported their hypothesis with a model study, in which baroclinic instability was the mechanism that produced the meandering path. The present results show that also the baro-

tropic instability can be an efficient mechanism producing basically the same internal oscillations.

It is worth emphasizing again that the interpretation of these modeling results proposed above reveals a strict connection between the bimodal path fluctuations of the Kuroshio south of Japan and the bimodal variability of the Kuroshio Extension, so that in the framework of the present model study one can speak of a self-sustained internal oscillation of the combined Kuroshio south of Japan–Kuroshio Extension system. Qiu and Chen (2005) have recently argued that the meridional path change of the KE jet is independent of the bimodal Kuroshio path variability south of Japan: in view of our analysis, on the other hand, experimental confirmation of a possible connection should be pursued.

b. Comparison with altimetric measurements

We have already noticed that the high and low energy states of the modeled variability are very similar to the elongated and contracted modes of the observed KE. We have also noticed that the manifestation of our self-sustained internal oscillation south of Japan is in basic agreement with the observed bimodal path fluctuations in the Kuroshio Current system. A more detailed comparison with observations will now be carried out with reference to a recent study of Qiu and Chen (2005, hereafter QC05), in which an unprecedented description of the KE variability based on an altimeter dataset (compiled by the CLS Space Oceanographic Division of Toulouse, France) that merges TOPEX/Poseidon, *Jason-1*, and *ERS-1/2* measurements, from October 1992 to December 2004, is presented.

To characterize in a simple and significant way KE changes, QC05 identified the instantaneous KE path as the SSH contour located near the maxima of the same field (which was found to correspond approximately to the 170-cm SSH level; the lines shown in the right column of Fig. 4 correspond to such paths). They then computed the pathlength $\ell(t)$ and the mean latitudinal position of the path $\langle\varphi\rangle(t)$ within different longitudinal ranges. We computed analogous quantities from our modeled data: in Figs. 5a,b $\ell(t)$ and $\langle\varphi\rangle(t)$ evaluated along the 15-cm SSH isoline (the contour that better approximates the maxima of the SSH in our case) are shown, respectively (they refer to the upstream KE, as, according to QC05, they are computed between 141° and 153°E). Therefore, Figs. 5a,b could in principle be compared with Figs. 4a, c of QC05, respectively.

The analysis of the upstream $\ell(t)$ allowed QC05 to define two distinct regimes: a stable mode (before May 1995 and after January 2002), in which the path is relatively short and is accompanied by a weak temporal variability, and an unstable mode (from mid 1995 to the end of 2001), in which the path is more convoluted (therefore longer) and exhibits monthly time-scale fluctuations resulting from the shedding and merging of mesoscale eddies. During the unstable mode the upstream $\langle\varphi\rangle(t)$ is also fluctuating over the same time scales and, moreover, a clear increasing trend is evident, $\langle\varphi\rangle$ passing from ~33.5° around 1997 to ~36.5° around 2001.

It is rather surprising to see that a very similar behavior is present also in our modeling results. Let us consider, for instance, the 10-yr-long period t = 143–153 yr whose synoptic evolution is shown in Fig. 4 and was discussed in detail in the previous subsection. With reference to Fig. 5 the correspondence t = 145 yr ↔ year 1993 and t = 153 yr ↔ year 2001 can be proposed. In fact, it is possible to identify a modeled unstable mode in the interval t = 147–153 yr (enclosed between two vertical dashed lines), within which (i) $\ell(t)$ has larger values and is accompanied by a strong variability, and (ii) $\langle\varphi\rangle(t)$ shows an increasing trend from ~33.5° at t ~ 148 yr to ~35° after ~5 yr (see section 4a for a discussion concerning the counterintuitive property for which a strong variability is associated with a weak jet, and vice versa). On the other hand, it is possible to identify a modeled stable mode in the interval t = 143–147 yr, within which the path is much less variable and has relatively small values, while $\langle\varphi\rangle$ shows a decreasing trend from ~35° to ~33.5° (this is the only substantial difference with the experimental values, since such a trend is found to last for only ~2 yr at the beginning of the unstable mode in the altimeter data). It is worth noticing that, as already found for the kinetic energies (see the beginning of section 4a), also the duration of the stable and unstable modes can vary significantly from cycle to cycle. For instance, as evidenced in Fig. 5, the stable and unstable modes just consider last ~4 and ~6 yr, respectively, while in the subsequent cycle they last ~6.5 and ~7.5 yr, respectively.

In conclusion, all the main features of the quantities $\ell(t)$ and $\langle\varphi\rangle(t)$ obtained from altimeter data in a stable and subsequent unstable mode find a significant quantitative correspondence in amplitude, variability, trend and timing with the corresponding ones obtained by the present model study. It is now possible to trace the stable and unstable modes just discussed in the modeled self-sustained oscillation interpreted in the preceding subsection. The stable mode as defined by QC05 corresponds, in our model results, to the phase during which the Kuroshio south of Japan yields a strong recirculation gyre and cyclonic meander and the Kuroshio Extension has a stable well-developed meandering pattern, but also to the phase in which the cyclonic

meander is eroded and the Kuroshio Extension kinetic energy reaches its minimum. The unstable mode, on the other hand, corresponds to the phase during which the Kuroshio Extension recharges, together with the recirculation gyre and cyclonic meander south of Japan.

The last, fundamental comparison that is still to be carried out is between the modeled 2D SSH maps and the corresponding maps obtained from altimeter data by QC05. If the correspondence $t = 145$–153 yr $\leftrightarrow$ years 1993–2001 established successfully for the parameters $\ell(t)$ and $\langle\varphi\rangle(t)$ turned out to be basically correct also for synoptic SSH signal, then one would be allowed to deduce that the present simple model does capture the main features of the Kuroshio Extension low-frequency variability. This appears to be indeed the case, as we will now discuss.

In the next comparisons (made every two years starting from $t = 145$ yr), m. stands for modeling data shown by the maps in the left column of Fig. 4, and o. stands for observations, referring to the maps of Fig. 2 of QC05. Here, in $t = 145$ yr, year 1993, two main crests are present in the KE in both m. and o.; their position and relative strength also compare well. The third weak crest present in m. appears as an extension of the second one in the o. The cyclonic meander south of Japan is pronounced, but more in m. than in the o.; in $t = 147$ yr, year 1995, the meander south of Japan has disappeared in both m. and o.; the Kuroshio extends east of 141°N without any appreciable meandering up to ~147°E in both m. and o., whereby a weak cyclonic meander appears in both m. and o. (but in m. it is more energetic and extending more to the north). More eastward an anticyclonic meander is present in m. and it is weaker in o. In $t = 149$ yr, year 1997, the cyclonic meander south of Japan is formed again in both m. and o., but it is more intense in m. The KE is in the form of three weak undulating meanders in both m. and o., whose positions are in good agreement. In $t = 151$ yr, year 1999, the KE has intensified considerably and now presents three well-defined meanders whose position, shape, and relative strength compare surprisingly well in m. and o. South of the first meander, a cyclonic retroflection is present in both m. and o., but is stronger in o. In $t = 143$ yr (virtually indistinguishable to $t = 153$ yr), year 2001, the cyclonic meander south of Japan is very intense in both m. and o.; in the KE, three intense anticyclonic meanders are present in m.; they are present in o. as well, although the third one is located more eastward and the first one is deformed by the presence of a small cyclonic gyre south of it (also in m. such a dipole structure is apparent, but the cyclonic circulation is much weaker). In conclusion, taking into account the simplicity of the model, the time-independent nature of the forcing, and the lack of topographic variations or baroclinic instability mechanism, the comparison between the modeled variability and the observed one is very good as far as a variety of dynamical features and their timing are concerned. This is extremely unlikely to be fortuitous; consequently, the hypothesis that the bimodal decadal variability of the KE is basically caused by a self-sustained chaotic oscillation related to the barotropic instability of the Kuroshio south of Japan without any crucial intervention of Sverdrup transport fluctuations or topographic interactions can be put forward.

c. *Preliminary analysis of the low-frequency variability in the framework of nonlinear dynamical systems theory*

Besides the physical interpretation of the fluid dynamical mechanisms responsible for the self-sustained oscillations (proposed in section 4a), use can also be made of the interpretative tools of the theory of nonlinear dynamical systems (see section 1) in order to gain deeper insight into the internal low-frequency variability of the KE produced by the present model. This task, however, is far beyond the aim of the present investigation. In this subsection we will limit ourselves to establish the basis for an analysis of this nature that will be carried out in future studies.

Figure 7a shows the time series of the kinetic energy E_K of the KE (i.e., integrated in section A) obtained for different values of the lateral eddy viscosity coefficient K_H, all for $\alpha = 1$ [see Eq. (2)], while Fig. 7b shows the time series of E_K obtained for different values of the amplitude of the forcing α, all for $K_H = 220\ \mathrm{m^2\ s^{-1}}$. The time series shown in Fig. 3a for sector A, but limited to 200 yr, can be identified both in Fig. 7a (fifth from top) and in Fig. 7b (fourth from top). Figures 8 and 9 show orbits projected onto the E_K (sector B)–E_K (sector A) and E_P (sector A $\cup$ B)–E_K (sector A $\cup$ B) planes, respectively, for different values of K_H.

Let us begin by considering the behavior for different values of the later eddy viscosity. Three types of low-frequency variability can be detected within the range $K_H = 400$–$200\ \mathrm{m^2\ s^{-1}}$: (i) a stationary state that changes into small amplitude, low energy chaotic oscillations after an initial Hopf bifurcation and successive period-doubling bifurcations; (ii) a large amplitude chaotic oscillation that we may define as of the KE-type; (iii) a small amplitude, intermediate energy periodic oscillation. These three types of variability are interconnected, and this suggests that we are in the presence of global bifurcations and homoclinic and heteroclinic orbits (e.g., Meacham 2000; Nadiga and Luce 2001; Si-

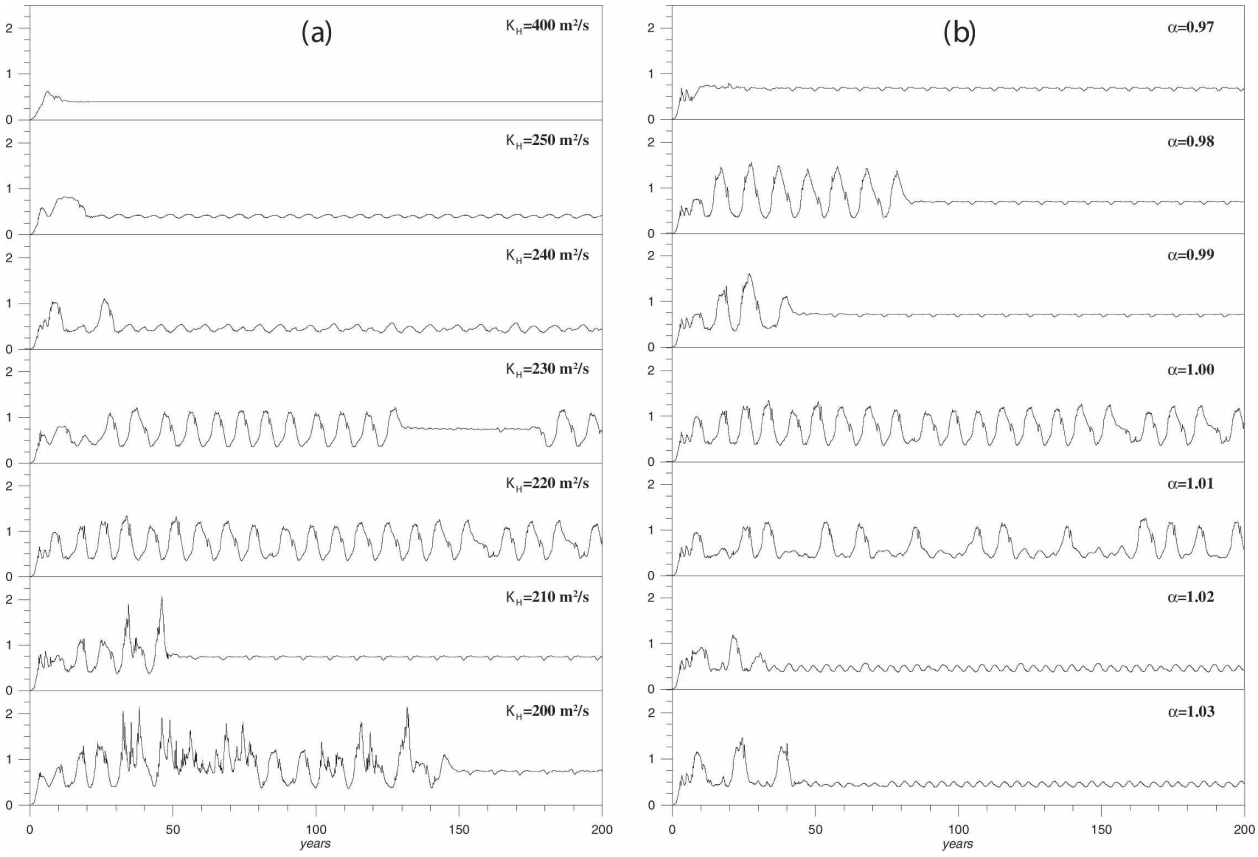

FIG. 7. Time series of the kinetic energy E_K integrated in sector A for different values of K_H with (a) $\alpha = 1$, and for different values of α with (b) $K_H = 220\ \mathrm{m^2\,s^{-1}}$.

monnet et al. 2003b, 2005; Dijkstra 2005), as we will discuss.

Let us begin with the first kind of variability: for sufficiently high values of K_H the internal variability disappears, while oscillatory gyre modes of type (i) arise after the first Hopf bifurcation, found just below $K_H = 400\ \mathrm{m^2\,s^{-1}}$ (see the fixed point in Fig. 8a corresponding to this value), when the nonlinear saturation of the linear instability of the stationary solution occurs. More and more complex time-dependent structure is then found for further decrease of K_H, associated with the classical route to chaos through successive period-doubling bifurcations. For $K_H = 250\ \mathrm{m^2\,s^{-1}}$ the variability, after spinup, is an aperiodic oscillation whose amplitude approximately doubles for $K_H = 240\ \mathrm{m^2\,s^{-1}}$ (see Fig. 7a and the clouds in Figs. 8a,b). The spatial structure of variability (i) resembles the state at $t = 148$ yr shown in Fig. 4, corresponding to the weakest phase (contracted mode) of the self-sustained oscillation discussed in the previous subsections.

Category (ii) refers to the variability discussed in sections 4a, b: it starts manifesting itself already for $K_H = 240\ \mathrm{m^2\,s^{-1}}$ at $t \approx 25$ yr, when a single oscillation substantially equal to that discussed in section 4a is found (represented by the convoluted line emerging from the cloud in Fig. 8b). The system then returns immediately to the small amplitude oscillations of type (i), this being a symptom that a global bifurcation has occurred. A further decrease of viscosity ($K_H = 230\ \mathrm{m^2\,s^{-1}}$) allows for several (~12) KE-type oscillations, after which ($t \approx$ 130 yr) the solution is attracted by a small amplitude limit cycle of intermediate energy [here termed as of category (iii) and resembling the stable phase of the KE at $t = 145$ yr shown in Fig. 4], presumably produced by a Hopf and successive period-doubling bifurcations originating from a fixed point falling in the same region of phase space. The system then returns back to the variability (ii) at $t \approx 175$ yr. This sudden transition between two kinds of variability of completely different character in the double-gyre problem was observed, for instance, by Simonnet et al. (2003b, see their Fig. 6, lower panel). Figure 8c helps understanding this transition: the portion of the orbit projected onto the E_K (sector B)–E_K (sector A) plane corresponding to the intermediate energy oscillation during the interval $t \approx$ 130–175 yr is contained in the oval, and is disconnected

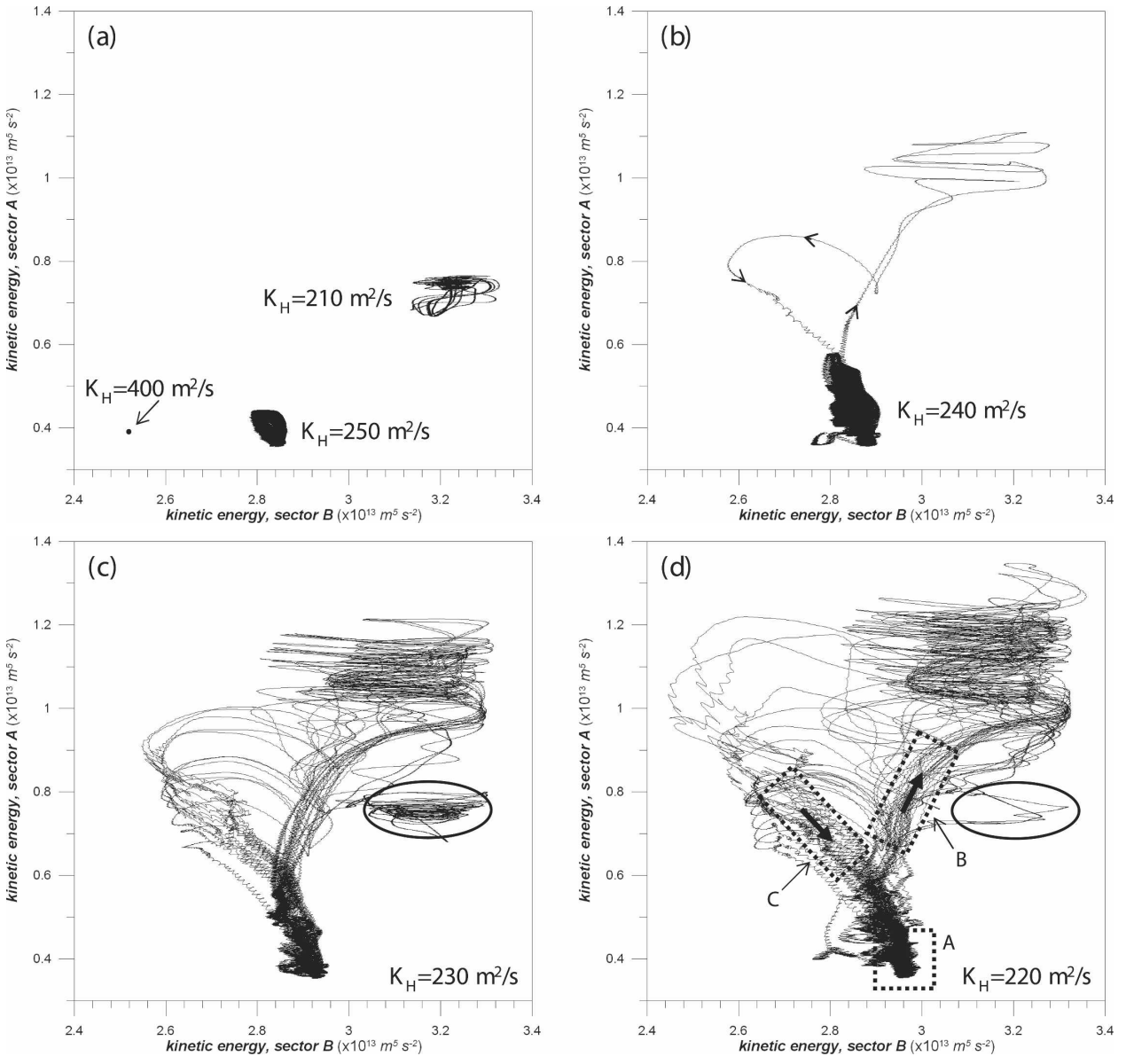

FIG. 8. Projection of flow trajectories onto the E_K (sector B)–E_K (sector A) plane for different values of the lateral eddy viscosity ($\alpha = 1$). (a) Orbits for $K_H = 400$ m^2 s^{-1} relative to the interval $t > 20$ yr, for $K_H = 250$ m^2 s^{-1} relative to the interval $t = 30$–200 yr, and for $K_H = 210$ m^2 s^{-1} relative to the interval $t > 55$ yr. (b) Orbit for $K_H = 240$ m^2 s^{-1} relative to the interval $t = 20$–200 yr; the arrows indicate the direction of evolution of the orbit. (c) Orbit for $K_H = 230$ m^2 s^{-1} relative to the interval $t = 20$–200 yr (the portion of the orbit enclosed in the oval is relative to the interval $t = 132$–175 yr). (d) Orbit for $K_H = 220$ m^2 s^{-1} relative to the interval $t = 20$–200 yr. The portion of the orbit enclosed in the oval is relative to the two intervals $t \approx 155.6$–158.3 yr and $t \approx 188.2$–190 yr. It is conjectured that the region A includes a saddle fixed point and regions B and C are portions of its unstable and stable manifolds, respectively.

from the KE-type strange attractor, but it licks it. The chaotic nature of the flow allows for an excursion into the basin of attraction of variability (iii), on which the orbit can reside for some time, but it eventually goes back where it came from: this suggests that (iii) is a saddle limit cycle. It is interesting to notice that the transition from variability (ii) to (iii) occurs when the oscillation, in terms of the kinetic energy integrated in sector A, presents an anomalously long intermediate energy state such as, for instance, the case shown in Fig. 5d for $t \approx 155$–158 yr: for this interval (and for another anomaly of this kind at $t \approx 188$–190 yr) the orbit for $K_H = 220$ m^2 s^{-1} (Fig. 8d) is indeed contained in the same region of phase space. At this value of viscosity,

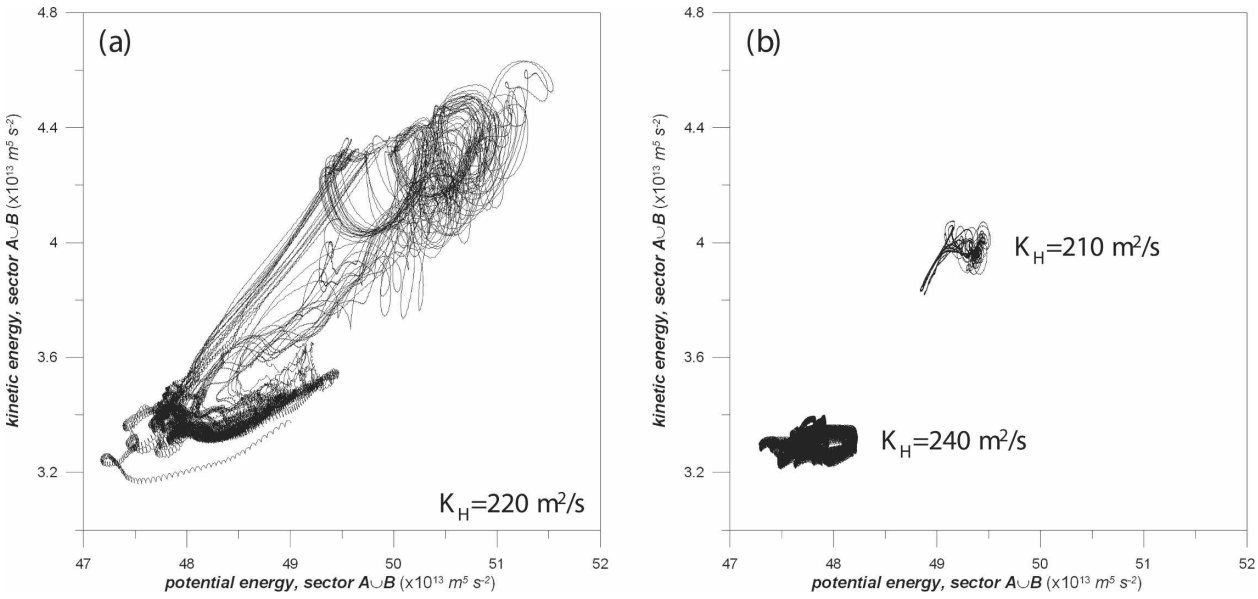

FIG. 9. Projection of flow trajectories onto the E_P (sector A $\cup$ B)–E_K (sector A $\cup$ B) plane for different values of the lateral eddy viscosity ($\alpha = 1$). (a) Orbit for $K_H = 220$ m^2 s^{-1} relative to the interval $t = 20$–200 yr. (b) Orbits for $K_H = 240$ m^2 s^{-1} relative to the interval $t = 33$–200 yr, and for $K_H = 210$ m^2 s^{-1} relative to the interval $t > 55$ yr.

however, it immediately goes back to the KE chaotic attractor: in fact, no transition from (ii) to (iii) was observed in the 400-yr long time series shown in Fig. 3a. For smaller values of viscosity ($K_H = 210$–200 m^2 s^{-1}) the KE-type variability soon degenerates into very large amplitude, highly chaotic oscillations that are then attracted by the variability of type (iii), where they lie at least up to $t = 200$ yr. Finally, Fig. 9 shows the strange attractor of the KE type (Fig. 9a) and the attractors for two other values of K_H in the E_P (sector A $\cup$ B)–E_K (sector A $\cup$ B) plane. The solutions for different values of the amplitude parameter (Fig. 7b) yield, again, transitions from KE-type oscillations to small amplitude oscillations of type (i) ($\alpha = 1.01, 1.02, 1.03$) and (iii) ($\alpha = 0.98, 0.99$). It is perhaps unexpected that a weaker forcing leads to higher energy oscillations [of type (iii)] while a stronger forcing leads to lower energy oscillations [of type (i)], but this somewhat counterintuitive behavior must be associated with the specific topological properties of phase space in the direction of varying forcing amplitude about the KE-type variability.

On the basis of the preceding analysis we conjecture that the KE-type chaotic oscillation (ii) obtained for $K_H = 220$ m^2 s^{-1} is a homoclinic orbit in phase space resulting from a global bifurcation associated with the reconnection of the stable (part of which is contained in region C of Fig. 8d) and unstable (part of which is contained in region B of Fig. 8d) manifolds of the saddle fixed point presumably located inside region A of Fig. 8d and corresponding to the contracted mode of the KE. Moreover, we conjecture that the sudden transitions between two kinds of variability found for $K_H = 230, 240$ m^2 s^{-1} with $\alpha = 1$ and for $K_H = 220$ m^2 s^{-1} with $\alpha = 0.98, 0.99, 1.01, 1.02, 1.03$ are due to heteroclinic connections. These are fascinating aspects of the extremely complex structure of phase space in the vicinity of what was termed the KE-type attractor, that deserve to be considered in detail in future studies.

In light of what is examined here, and in relation to the choice of K_H made for our study of the KE, it should be stressed that there is obviously no reason to prefer a priori any of the values of the lateral eddy viscosity coefficient within the realistic range 200–400 m^2 s^{-1}, but analysis of the numerical solutions has evidenced that the large amplitude variability [of type (b)] obtained for values $K_H = 220$–230 m^2 s^{-1} shows striking similarities with the observed one, while the other two kinds of variability [of type (i) and (iii)] are completely out of range as far as the oscillation amplitude is concerned. For this reason one of those two values of K_H had to be chosen. The value $K_H = 220$ m^2 s^{-1} was then adopted because it insured a stable (though chaotic) oscillation without "global" transitions to other regimes. However, it should be pointed out that this last choice is more due to esthetical rather than substantial reasons, since there is no experimental evidence that such transitions do not occur in the real oceans. It is remarkable, as we have noticed many times in this paper, that this model captures so well the variability of

the real Kuroshio Extension as observed during approximately one cycle (from 1992 to 2004), but it is also interesting to notice that the same model evidences the ability to temporary transitions from that variability to different kinds of behaviors (particularly interesting to this respect is the case $\alpha = 1.01$ shown in Fig. 7b). Long-term changes of the variability studied in this paper are one of the most relevant aspects that should be analyzed in future studies.

5. Conclusions

It is rather surprising that this simple reduced-gravity model of the Kuroshio Extension system, which includes elements of realism (such as a wind based on climatology, a domain of integration with the correct extension and a schematic coastline) but that, however, is forced by a time-independent wind and does not include neither topographic interactions nor the baroclinic instability mechanism, is nonetheless able to produce a mean jet and a decadal variability that capture the main features of the real Kuroshio Extension as observed by in situ and altimeter data.

This is surprising for at least three reasons. The first reason is that the mean meandering pattern of the Kuroshio Extension is usually interpreted as the result of topographic effects, either through interaction of the flow with the Izu Ridge, giving rise to lee-wave meanders (Mizuno and White 1983), or/and through steering by eddy-driven mean abyssal currents (Hurlburt et al. 1996; Mitchell et al. 1996). The present modeling results show, on the other hand, that purely nonlinear intrinsic effects without the intervention of any topographic interaction, can account for a mean meandering Kuroshio Extension in significant agreement with observations.

The second reason is that the observed, very strong low-frequency variability of the Kuroshio Extension is usually considered as the response to a time-dependent atmospheric forcing (e.g., Miller et al. 1998; Deser et al. 1999; Qiu 2002, 2003; Qiu and Chen 2005). Here, on the other hand, we have shown that a time-independent climatological wind produces an internal decadal self-sustained chaotic oscillation whose resemblance with the real variability as observed through satellite altimeters during the last 12 yr (Qiu and Chen 2005) is amazing. Although it is well known that an atmospheric double-gyre system can produce oceanic low-frequency variability, most of the numerical studies on the double-gyre problem were intended to represent the Gulf Stream (mainly due to a limited extension of the domain that could not allow for a sufficiently strong Sverdrup return flow for the Pacific), while the Kuroshio Extension did not receive analogous attention. In a recent study on the mechanisms of decadal variability of the wind-driven ocean circulation, Hogg et al. (2005) suggested that nonlinear mechanisms could explain the observed decadal variability of the Kuroshio Extension, although their model could not allow for such a direct comparison. The present model study is in line with the indications of those authors.

The third reason is that, even assuming that the basic mechanisms of formation of the mean Kuroshio Extension and of its decadal variability are indeed the ones included in our model, the good performance of such a simple model implementation is somewhat unexpected. This shows that a generalization of the classical rectangular box beta-plane double-gyre system to an implementation that includes a realistic domain size, a correct value of the Coriolis parameter at any latitude, a wind field inspired by real data and, last but not least, a schematic western coastline is able to produce (always within the framework of a process study) a free inertial jet directly comparable with observations, provided, of course, that none of the fundamental effects be excluded from the governing equations. Observing that the nonlinear theory of the internal variability of the wind-driven ocean circulation is now entering a mature stage so that predictive power with respect to low-frequency behavior can be claimed, Simonnet et al. (2005) suggest that in the future this theory needs to be expanded to models that capture additional processes such as stratification, bottom topography, and time-dependent wind and buoyancy forcing. We feel that in addition to those extensions, complementary studies would be worth carrying out in which more realistic (but still idealized) geometry and forcing should be introduced, while keeping the dynamical effects at their simplest level in the governing equations. In doing so one could discover (as done in this paper) that in some cases even a very simple modeled ocean can capture (and at a significant level) observed relevant features of the real midlatitude ocean dynamics.

The obvious conclusion we feel we can draw from this model study is that the bimodal decadal variability of the Kuroshio Extension is likely to be basically due to a self-sustained internal oscillation related to the instability of the Kuroshio south of Japan, without any crucial intervention of Sverdrup transport fluctuations and of topographic interactions, although such effects may well play an important role in shaping the finer structure of Kuroshio Extension changes. Future modeling studies will be needed to further support this hypothesis.

The validity of this hypothesis may have important climatological implications related to the decadal variability of the midlatitude North Pacific region and,

more specifically, to the Pacific Decadal Oscillation. The Kuroshio Extension was recognized to play an active role in determining oscillations on a decadal time scale within the framework of coupled ocean–atmosphere models (e.g., Latif and Barnett 1994, 1996; Barnett et al. 1999; Schneider et al. 2002). Other studies stress the role of the atmosphere in inducing decadal changes in the Kuroshio Extension (e.g., Miller et al. 1998; Deser et al. 1999; Qiu 2003; Qiu and Chen 2005), which, in this perspective, plays a more passive role. On the other hand, to the best of the author's knowledge, the hypothesis that an internal oceanic mechanism be the main cause of the Kuroshio Extension decadal variability, and that the latter could in turn play a role in contributing to induce an analogous variability in the atmosphere has never been put forward. In view of the modeling results presented in this paper, we believe it would be worth investigating this possibility through the development of ad hoc process studies.

The physical interpretation of the self-sustained internal oscillation of the Kuroshio south of Japan–Kuroshio Extension system we proposed in section 4a includes a series of geophysical fluid dynamical processes that should be investigated more closely through, again, the development of ad hoc process studies. For example, we suggested that a meridionally elongated cyclonic meander south of Japan could act as a barrier between a nearly steady recirculation gyre to the west and a weakly dissipating Kuroshio Extension to the east, but only if the two anticyclonic vortices adjacent to the meander are sufficiently intense. Even a small variation in the intensity of any of the two gyres with respect to the nearly stable situation can lead to a rapid transition to quite different behaviors (namely, to the penetration of the Kuroshio deep into the Pacific or to the triggering of oscillations associated with the production of cold-core eddies). What are the basic mechanisms that produce this behavior, and how is this related to the various parameters included in the problem? Another process we identified that is not well understood is the one for which a weak Kuroshio Extension during its intensification is accompanied by a high level of eddy kinetic energy, while the latter becomes very low when the jet becomes strong (a rather counterintuitive behavior). This property was clearly observed by Qiu and Chen (2005) who interpreted it as the result of topographic interactions. Instead, such a process was considered here as an adjustment associated with the gradual intensification of the jet, but what are the actual dynamical mechanisms that produce this behavior? Mechanistic regional models should be developed in order to provide answers to these questions.

Among the possible future extensions of this study one can list analyses on the role played by baroclinic instability (by passing, e.g., to a 2.5-layer model, as done by Simonnet et al. 2003a,b), of topographic interactions (but this is much more computationally expensive, as the external mode should be included in the model), and of the effect of (seasonally, stochastically, etc.) varying winds on the low-frequency variability of the jet. Another important development concerns a thorough analysis of the structure of phase space of our dynamical system that we have only preliminarily started to investigate in section 4c, where we suggest that our modeled low-frequency variability corresponds to a homoclinic orbit. Shedding light on the extremely complex structure of phase space we found near our modeled Kuroshio Extension would also help interpreting the complex fluid dynamical processes that regulate the decadal variability of the jet.

Acknowledgments. I am pleased to thank Paola Malanotte-Rizzoli, for having introduced me to the double-gyre problem, and Bo Qiu, for his valuable comments and for having made available a manuscript (Qiu and Chen 2005) that allowed me to compare the low-frequency variability of the Kuroshio Extension produced by the model with the altimetric measurements of the last 12 yr.

REFERENCES

Barnett, T. P., D. W. Pierce, R. Saravanan, N. Schneider, D. Dommenget, and M. Latif, 1999: Origins of the midlatitude Pacific decadal variability. *Geophys. Res. Lett.,* **26,** 1453–1456.

Deser, C., M. A. Alexander, and M. S. Timlin, 1999: Evidence for a wind-driven intensification of the Kuroshio Current Extension from the 1970s to the 1980s. *J. Climate,* **12,** 1697–1706.

Dijkstra, H. A., 2005: *Nonlinear Physical Oceanography*. Springer, 532 pp.

Ghil, M., Y. Feliks, and L. U. Sushama, 2002: Baroclinic and barotropic aspects of the wind-driven ocean circulation. *Physica D,* **167,** 1–35.

Hogg, A. M., P. D. Killworth, J. R. Blundell, and W. K. Dewar, 2005: Mechanisms of decadal variability of the wind-driven ocean circulation. *J. Phys. Oceanogr.,* **35,** 512–531.

Hurlburt, H. E., A. J. Wallcraft, W. J. Schmitz, P. J. Hogan, and E. J. Metzger, 1996: Dynamics of the Kuroshio/Oyashio current system using eddy-resolving models of the North Pacific Ocean. *J. Geophys. Res.,* **101,** 941–976.

Jiang, S., F. Jin, and M. Ghil, 1995: Multiple equilibria, periodic and aperiodic solutions in a wind-driven, double-gyre, shallow-water model. *J. Phys. Oceanogr.,* **25,** 764–786.

Kelly, K., and S. T. Gille, 1990: Gulf Stream surface transport and statistics at 69°W from the Geosat altimeter. *J. Geophys. Res.,* **95,** 3149–3161.

Latif, M., and T. P. Barnett, 1994: Causes of decadal climate variability over the North Pacific and North America. *Science,* **266,** 634–637.

——, and ——, 1996: Decadal climate variability over the North

Pacific and North America: Dynamics and predictability. *J. Climate,* **9,** 2407–2423.
Levitus, S., 1982: *Climatological Atlas of the World Ocean*. NOAA Prof. Paper 13, U.S. Government Printing Office, Washington, DC, 173 pp.
McCalpin, J. D., and D. B. Haidvogel, 1996: Phenomenology of the low-frequency variability in a reduced-gravity, quasigeostrophic double-gyre model. *J. Phys. Oceanogr.,* **26,** 739–752.
Meacham, S. P., 2000: Low-frequency variability in the wind-driven circulation. *J. Phys. Oceanogr.,* **30,** 269–293.
Miller, A. J., D. R. Cayan, and W. B. White, 1998: A westward-intensified decadal change in the North Pacific thermocline and gyre-scale circulation. *J. Climate,* **11,** 3112–3127.
Mitchell, J. L., W. J. Teague, G. A. Jacobs, and H. E. Hurlburt, 1996: Kuroshio Extension dynamics from satellite altimetry and a model simulation. *J. Geophys. Res.,* **101,** 1045–1058.
Mizuno, K., and W. B. White, 1983: Annual and interannual variability in the Kuroshio current system. *J. Phys. Oceanogr.,* **13,** 1847–1867.
Nadiga, B. T., and B. P. Luce, 2001: Global bifurcation of Shilnikov type in a double-gyre ocean model. *J. Phys. Oceanogr.,* **31,** 2669–2690.
Nauw, J. J., and H. A. Dijkstra, 2001: The origin of low-frequency variability of double-gyre wind-driven flows. *J. Mar. Res.,* **59,** 567–597.
Niiler, P. P., N. A. Maximenko, G. G. Panteleev, T. Yamagata, and D. B. Olson, 2003: Near-surface dynamical structure of the Kuroshio Extension. *J. Geophys. Res.,* **108,** 1–24.
Nishida, H., 1982: Description of the Kuroshio meander in 1975–1980—Large meander of the Kuroshio in 1975–1980. *Rep. Hydrogr. Res.,* **17,** 181–207.
Pedlosky, J., 1987: *Geophysical Fluid Dynamics*. Springer-Verlag, 710 pp.
Pierini, S., 2003: A model of the wind-driven seasonal variability in the tropical North Pacific, with validation through altimeter data. *J. Phys. Oceanogr.,* **33,** 2156–2172.
——, 2005: A model study of the spectral structure of boundary-driven Rossby waves, and related altimetric implications. *J. Phys. Oceanogr.,* **35,** 218–231.
Qiu, B., 1995: Variability and energetics of the Kurosshio Extension and its recirculation gyre from the first two-year TOPEX data. *J. Phys. Oceanogr.,* **25,** 1827–1842.
——, 2000: Interannual variability of the Kuroshio Extension system and its impact on the wintertime SST field. *J. Phys. Oceanogr.,* **30,** 1486–1502.
——, 2002: The Kuroshio Extension system: Its large-scale variability and role in the midlatitude ocean–atmosphere interaction. *J. Oceanogr.,* **58,** 57–75.
——, 2003: Kuroshio Extension variability and forcing of the Pacific Decadal Oscillations: Responses and potential feedback. *J. Phys. Oceanogr.,* **33,** 2465–2482.
——, K. A. Kelly, and T. M. Joyce, 1991: Mean flow and variability in the Kuroshio Extension from *Geosat* altimetry data. *J. Geophys. Res.,* **96,** 18 491–18 507.
——, and W. Miao, 2000: Kuroshio path variations south of Japan: Bimodality as a self-sustained internal oscillation. *J. Phys. Oceanogr.,* **30,** 2124–2137.
——, and S. Chen, 2005: Variability of the Kuroshio Extension jet, recirculation gyre, and mesoscale eddies on decadal time scales. *J. Phys. Oceanogr.,* **35,** 2090–2103.
Rienecker, M. M., and L. L. Ehret, 1988: Wind stress curl variability over the North Pacific from the Comprehensive Ocean-Atmosphere data set. *J. Geophys. Res.,* **93,** 5069–5077.
——, R. Atlas, S. D. Schubert, and C. S. Willet, 1996: A comparison of surface wind products over the North Pacific Ocean. *J. Geophys. Res.,* **101,** 1011–1023.
Schmeits, M. J., and H. A. Dijkstra, 2001: Bimodal behavior of the Kuroshio and the Gulf Stream. *J. Phys. Oceanogr.,* **31,** 3435–3456.
Schneider, N., A. J. Miller, and D. W. Pierce, 2002: Anatomy of North Pacific decadal variability. *J. Climate,* **15,** 586–605.
Simonnet, E., M. Ghil, K. Ido, and R. Temam, 2003a: Low-frequency variability in shallow-water models of the wind-driven ocean circulation. Part I: Steady-state solution. *J. Phys. Oceanogr.,* **33,** 712–728.
——, ——, ——, and ——, 2003b: Low-frequency variability in shallow-water models of the wind-driven ocean circulation. Part II: Time-dependent solutions. *J. Phys. Oceanogr.,* **33,** 729–752.
——, ——, and H. Dijkstra, 2005: Homoclinic bifurcations in the quasi-geostrophic double-gyre circulation. *J. Mar. Res.,* **63,** 931–956.
Spall, M. A., 1996a: Dynamics of the Gulf Stream/deep western boundary current crossover. Part I: Entrainment and recirculation. *J. Phys. Oceanogr.,* **26,** 2152–2168.
——, 1996b: Dynamics of the Gulf Stream/deep western boundary current crossover. Part II: Low-frequency internal oscillations. *J. Phys. Oceanogr.,* **26,** 2169–2182.
Taft, B. A., 1972: Characteristics of the flow of the Kuroshio south of Japan. *Kuroshio—Its Physical Aspects*. H. Stommel and K. Yoshida, Eds., University of Tokyo Press, 165–216.
Teague, W. J., M. J. Carron, and P. J. Hogan, 1990: A comparison between the Generalized Digital Environmental Model and Levitus climatologies. *J. Geophys. Res.,* **95,** 7167–7183.
Tomczak, M., and J. S. Godfrey, 2002: *Regional Oceanography: An Introduction*. Pergamon, online ed., 391 pp.
Wyrtki, K., L. Magaard, and J. Hagar, 1976: Eddy energy in the oceans. *J. Geophys. Res.,* **81,** 2641–2646.